

Evidence of Subsurface Oxygen Vacancy Ordering on Reduced CeO₂(111)

Stefan Torbrügge* and Michael Reichling

Fachbereich Physik, Universität Osnabrück, BarbarasträÙe 7, 49076 Osnabrück, Germany

Atsushi Ishiyama, Seizo Morita, and Óscar Custance

Graduate School of Engineering, Osaka University, 2-1 Yamada-Oka, 565-0871 Suita, Osaka, Japan

(Received 24 January 2007; published 1 August 2007)

Surface and subsurface oxygen vacancies on the slightly reduced CeO₂(111) surface have been studied by atomic resolution dynamic force microscopy at 80 K. Both types of defect are clearly identified by the comparison of the observed topographic features with the corresponding structures predicted from recent first-principles calculations. By combining two simultaneously acquired signals (the topography and the energy dissipated from the cantilever oscillation), we are able to unambiguously locate subsurface oxygen vacancies buried at the third surface atomic layer. We report evidence of local ordering of these subsurface defects that suggests the existence of a delicate balance between subtle interactions among adjacent subsurface oxygen vacancy structures.

DOI: 10.1103/PhysRevLett.99.056101

PACS numbers: 82.65.+r, 68.35.Dv, 68.37.Ps, 82.47.Ed

Materials based on ceria (CeO₂) hold substantial promise in diverse research areas such as catalysis and solid-fuel cell technology, mainly for the production of hydrogen [1]. In this context, ceria acts as an oxygen buffer as well as promoting noble-metal catalytic activity [1,2]. This important capability for storing and releasing oxygen is a result of the rapid formation and elimination of oxygen vacancy defects [1]. These defects at slightly and strongly reduced CeO₂(111) surfaces—the thermodynamically most stable crystallographic termination of ceria [3]—have been studied by means of both scanning tunneling microscopy (STM) [4–6] and dynamic force microscopy (DFM) [7–10]. Although it is possible to explore ceria surfaces using STM while heating the sample at elevated temperatures [6] (working at the very limit of this technique), DFM operated in the so-called non-contact mode (NC-AFM) [11–13] rises as the natural method for the characterization of atomic defects [7–9] and adsorbates [10] at the surfaces of this wide band-gap (6 eV) oxide. Recent STM studies on the reduced CeO₂(111) surface established that one subsurface oxygen vacancy is required to nucleate linear surface oxygen vacancy clusters [6]. Thus, these subsurface vacancies seem to play a fundamental role in the catalytic properties of ceria by enabling a further surface oxygen release and stabilizing the formation of linear oxygen vacancy clusters, which are the dominant defect structures on the strongly reduced surface [6–8]. There is, however, a notable lack of experimental information about the structure, stability, and behavior of these subsurface oxygen vacancies, mainly because of the difficulties to observe and precisely locate them.

In this Letter, we elucidate the structure of oxygen vacancies in the slightly reduced CeO₂(111) surface using DFM at low temperatures, focusing on the subsurface vacancies. We clearly identify surface and subsurface oxygen vacancies and corroborate the topography predicted by

recent first-principles calculations [14]. We present a method to precisely determine the location of subsurface oxygen vacancies using an atomic force microscope (AFM), and data pointing towards the existence of interactions between subsurface oxygen vacancy structures that make them to order in open linear arrays upon the presence of a high density of these defects.

Experiments were carried out with a home-built ultra-high vacuum AFM [15] operated [16] at low temperature (80 K) with the frequency modulation detection method [17], keeping the cantilever oscillation amplitude constant and the tip-surface electrostatic interaction minimized [18]. Tip preparation is described elsewhere [19]. The CeO₂(111) surface (Commercial Crystal Laboratories) was prepared *in situ* by repeating cycles of Ar⁺ ion sputtering (1 kV, 4×10^{-5} Torr, 10 min) at room temperature with subsequent annealing of the sample for 2 minutes at 1225 K. We checked that this protocol produces LEED patterns showing the characteristic hexagonal spots of the (1 × 1) surface termination [5]. During the final annealing of the surface preparation, the pressure was kept below 2×10^{-9} Torr. After typically 30 minutes of cooling down at room temperature at a pressure below 5×10^{-10} Torr, the sample was transferred to the low temperature AFM, and the DFM experiments were conducted at a base pressure below 3×10^{-11} Torr.

Figure 1 shows the typical topography ascribed to a surface and a subsurface oxygen vacancy at the CeO₂(111) surface. In our images, the surface oxygen vacancy [Fig. 1(a)] can be recognized as a missing atom surrounded by six atoms that protrude about 12 pm [see Fig. 1(c)] from the unperturbed layer of oxygen atoms in which the surface is terminated. This height difference well agrees with the vertical displacement predicted by first-principles calculations for the six oxygen atoms next to a surface vacancy [14]. The results from these calculations

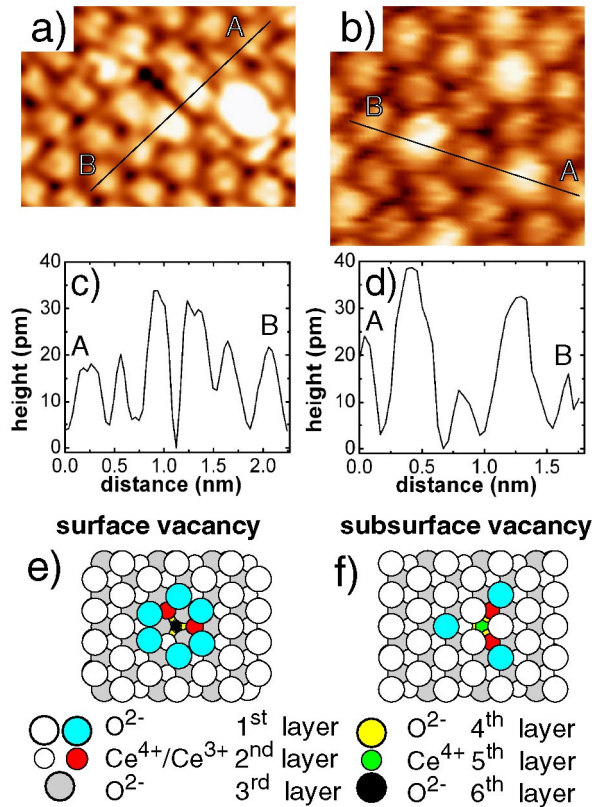


FIG. 1 (color online). DFM topographic images of a surface (a) and a subsurface (b) oxygen vacancy, together with the corresponding height profiles (c) and (d) and structural models (e) and (f), respectively. The protrusion at the right side of the surface oxygen vacancy (a) is ascribed to a hydroxide group substituting a surface oxygen [10]. The normalized frequency shift [23] image set points were $-7.5 \text{ fN}\sqrt{m}$ for (a) and $-2.9 \text{ fN}\sqrt{m}$ for (b), respectively [24].

also predict a slight lateral relaxation of the atoms surrounding the vacancy that tend to form pairlike structures [see the model in Fig. 1(e)], an effect observed in our images as well [see Fig. 1(a)]. According to this theoretical calculation, the two excess electrons left from the missing surface oxygen ion are localized at two of the three Ce^{4+} ions of the second layer next to the vacancy, which become Ce^{3+} ions [14].

The appearance of the subsurface oxygen vacancies in our images [Fig. 1(b)] is as three oxygen atoms protruding approximately 20 pm from the surface [Fig. 1(d)] and spaced by two lattice constants, while the three inner oxygen atoms separated by one lattice constant being slightly relaxed towards the bulk [Fig. 1(d)]. We have been able to identify these subsurface oxygen vacancies because of the excellent agreement of the observed topographic features with predictions from first-principles calculations for the structure and relaxations expected at the surface, induced by the lack of an oxygen atom two layers below the surface plane (third surface atomic layer) [14] [see the model in Fig. 1(f)]. In the case of the subsurface oxygen vacancy,

calculations predict that the two excess electrons are also localized at two of the three Ce^{4+} ions of the second surface layer next to the defect, which turn to Ce^{3+} ions [14]. This charge localization produced a local symmetry breaking and might play an important role on the ordering of these defects under a high concentration situation, as discussed below.

It is still under discussion whether the structure associated with a surface oxygen vacancy is energetically more favorable than the one ascribed to a subsurface oxygen vacancy [3,14]. While STM experiments performed at elevated sample temperatures suggest that both defects are equally distributed [6], our results indicate variability in the distribution of surface and subsurface oxygen vacancies from terrace to terrace over the same surface, with regions where almost no subsurface oxygen vacancies are found and other surface areas where a high concentration of them can be clearly observed. A topographic image of a terrace dominated by subsurface oxygen vacancies is depicted in Fig. 2(a). A large amount of protruding oxygen

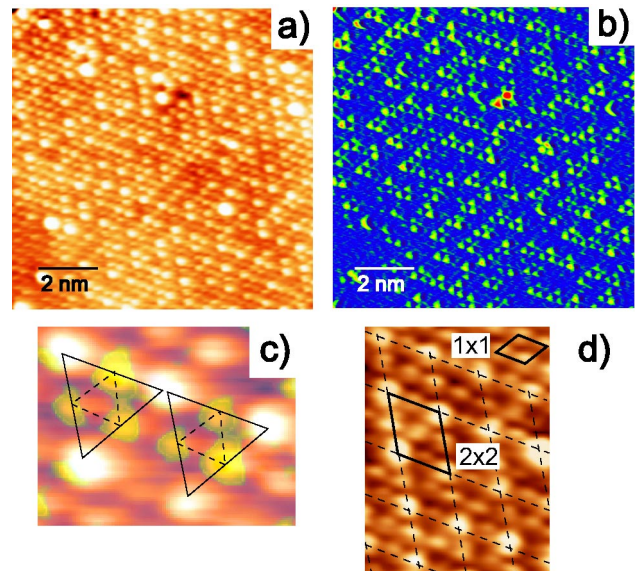


FIG. 2 (color online). Topographic (a) and dissipation (b) images of a slightly reduced $\text{CeO}_2(111)$ surface area. (c) Detail of two adjacent subsurface oxygen vacancies where the corresponding dissipation signal has been superimposed to the topography, merging two images in a single frame. Solid and dashed triangles indicate the characteristic contrast pattern in topography and dissipation signal, respectively. (d) Surface area of $(2.5 \times 3.5) \text{ nm}^2$ showing protruding oxygen atoms associated with subsurface oxygen vacancy structures in a (2×2) local arrangement; the unit cells of the two observed periodicities and the dashed grid with the (2×2) periodicity are also depicted. The image set point was $-2.9 \text{ fN}\sqrt{m}$. The average maximum value of the dissipation signal associated with the subsurface oxygen vacancy structures in (b) is 0.34 eV/cycle ; the maximum dissipation signal in the image corresponds to 0.53 eV/cycle , and it is located over the two surface oxygen vacancies nearby a hydroxide defect pointed out in Fig. 3(b).

atoms makes it difficult to identify the subsurface oxygen vacancies upon a first inspection. However, we are able to unambiguously locate the exact position of the subsurface oxygen vacancies by looking at the simultaneously recorded dissipation signal, which is related to the amount of energy lost by the cantilever due to nonconservative interactions with the individual surface atoms [20,21]. Figure 2(b) shows the corresponding dissipation signal to the topographic image depicted in Fig. 2(a). A comparison between both signals over the same surface area reveals that each group of three protrusions apparent on the dissipation image exactly match with the lattice positions of the three inner surface oxygen atoms just above the subsurface oxygen vacancy [Fig. 1(f)]. This is clearly seen in Fig. 2(c), where the dissipation signal registered for two adjacent subsurface oxygen vacancy structures is superimposed to the corresponding topography. For clarity, the protrusions observed in topography and dissipation images have been highlighted by solid and dashed triangles, respectively. This comparison makes it also clear that the oxygen atoms protruding in topography exhibit almost no contrast in dissipation.

The enhancement of dissipation signal over the three inner surface oxygen atoms above the subsurface vacancy has important implications regarding the stability of the associated surface structure that might be of relevance for the catalytic properties of the $\text{CeO}_2(111)$ surface. The presence of atomic contrast in the dissipation signal is related to considerable vertical relaxations of the probed surface atom between its minimal adsorption energy configuration and a metastable energy minimum slightly above the surface plane created due to the interaction with the apex of the AFM tip [20,21]. In this context, the stronger dissipation signal registered over these three atoms suggests that they are more weakly bonded than the other surface oxygen atoms. This fact is very plausible considering the lack of coordination by the absence of an oxygen atom two layers below and the corresponding redistribution of the excess electrons on the Ce^{3+} ions [14]. This finding may imply that the oxygen release from the surface could take place preferentially at these three atomic positions above the subsurface oxygen vacancy (especially at elevated temperatures), with the consequent formation of a dimer defect or more complex structures [6].

The ability to identify the exact location of subsurface oxygen vacancies allows us to obtain further information about these defects. In Fig. 3, the position and type of defect found in the surface area shown in Fig. 2(a) are depicted. Upon the topographic image, the protruding oxygen atoms of the subsurface oxygen vacancy structures seem to decorate almost the whole terrace generating a (2×2) pattern [see detail in Fig. 2(d)], likely to be confused, at a first glance, with a local surface reconstruction. The dissipation image [Fig. 3(b)] clearly reveals, however,

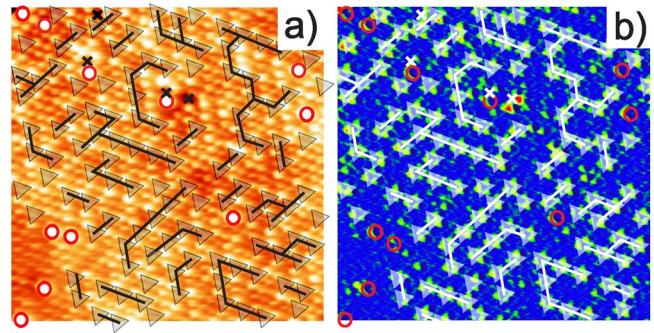


FIG. 3 (color online). Images shown in Figs. 2(a) and 2(b) where the association between the observed surface structure and the type of defect has been depicted. Triangles, crosses, and circles correspond to subsurface oxygen vacancies, surface oxygen vacancies, and hydroxide defects [10], respectively. The lines over both images highlight the arrangement observed for the subsurface oxygen vacancy structures.

that the subsurface oxygen vacancy structures seem to follow a linear arrangement leaving some space between them [Fig. 3], instead of condensing into close packing. In our images, no nearest neighbor subsurface oxygen vacancies have been detected, and the minimum spacing between adjacent defects is two lattice constants.

This open linear patterning resembles the one observed in some heterogeneous surfaces where a delicate balance of short-range interactions between the constituent atoms determines the geometry [22], and it points towards the existence of an interaction between adjacent subsurface oxygen vacancy structures.

A detail of the local linear ordering of these subsurface oxygen vacancies is displayed in Fig. 4. The structures associated with the subsurface oxygen vacancies are highlighted by triangles in both the topographic [Fig. 4(a)] and dissipation [Fig. 4(b)] image. A surface area free of any defect between the two lines of subsurface vacancies is clearly seen in the dissipation image in contrast with the topography, where the presence of a subsurface oxygen

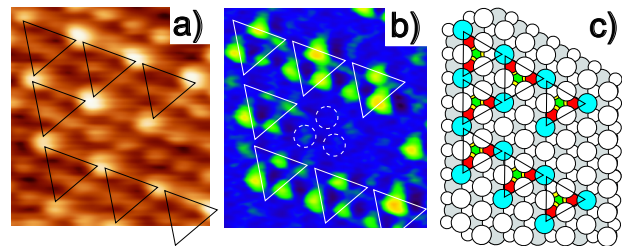


FIG. 4 (color online). Topography (a) and dissipation (b) images together with the corresponding schematic model (c) of the typical local ordering of subsurface oxygen vacancies observed in our images. The subsurface oxygen vacancy structures are highlighted by triangles. The dashed circles indicate a defect free surface area. The color coding of the model depicted in (c) is the same as in Fig. 1. The image set point was $-2.9 \text{ fN}\sqrt{m}$.

vacancy would be expected at the atomic sites pointed out by the three dashed circles in Fig. 4(b). Assuming the charge localization at the Ce^{3+} ions shown in Fig. 1(f) predicted by first-principles calculations [14], it is possible to arrange the subsurface vacancy structures in such a geometry that the protruding surface oxygen atom above three Ce^{4+} ions [Fig. 1(f)] would interact with one of the Ce^{3+} ions of the adjacent subsurface oxygen vacancy structure, as depicted in the proposed atomic model for this surface area [Fig. 4(c)]. For all the linear patterns highlighted in the image shown in Fig. 3, it is possible to perform a similar ordering of the relative position of the protruding surface oxygen atoms and the Ce^{3+} ions so that each protruding surface oxygen interacts with a single Ce^{3+} ion at the second surface layer. This seems to be the preferred situation since only a 15% of subsurface oxygen vacancy structures has been found disconnected from any other linear pattern, and, for all the linear patterns in Fig. 3, there is only a 8% of protruding oxygen atoms that would not have a Ce^{3+} ion as a nearest neighbor in the second surface layer. Although the origin of these open linear arrangements is unknown, we speculate that it might be related to a subtle balance of attractive and repulsive interactions between adjacent subsurface oxygen structures. In this context, a preference of each protruding surface oxygen atom to be in close proximity with one of the Ce^{3+} ions of the second surface layer—reducing the local symmetry breaking imposed by the charge localization—could account for the short-range attractive interaction. This attraction would compete with a short-range repulsion—possibly of an electrostatic origin [3]—that would prevent the formation of nearest neighboring subsurface oxygen vacancies, a situation that has been not observed.

In summary, we have identified surface and subsurface oxygen vacancies on the slightly reduced $\text{CeO}_2(111)$ surface by means of dynamic force microscopy operated at low temperature. The topographic features we have registered for these defects fully corroborate the corresponding structures and topography predicted by previously reported first-principles calculations [14]. By combining two complementary signals, namely, the topography and the dissipation, we are able to unambiguously locate oxygen vacancies buried at the third surface atomic layer. Our findings indicate that, upon a high enough concentration of subsurface oxygen vacancies, these defects do not arrange in a close layout but appear in ordered arrays with a tendency to form linear patterns, leaving defect free areas in between. These arrays might be consequence of a delicate balance between attractive and repulsive interactions among subsurface oxygen vacancy structures. We hope that our results would stimulate further investigations to elucidate the origin and true nature of the interactions that produce these linear arrays.

We are grateful to S. Fabris and F. Esch for stimulating discussions. This work was supported by the 21st COE program and by a Grant in Aid for Science Research, Special Coordination Funds from the MEXT of Japan, and the DFG-JSPS international cooperation program.

*storbrue@uos.de

- [1] A. Trovarelli, *Catal. Rev. Sci. Eng.* **38**, 439 (1996).
- [2] Q. Fu, H. Saltsburg, and M. Flytzani-Stephanopoulos, *Science* **301**, 935 (2003).
- [3] Z. X. Yang, T. K. Woo, M. Baudin, and K. Hermansson, *J. Chem. Phys.* **120**, 7741 (2004).
- [4] H. Nörenberg and G. A. D. Briggs, *Phys. Rev. Lett.* **79**, 4222 (1997).
- [5] H. Nörenberg and G. A. D. Briggs, *Surf. Sci.* **402**, 734 (1998).
- [6] F. Esch, S. Fabris, L. Zhou, T. Montini, C. Africh, P. Fornasiero, G. Comelli, and R. Rosei, *Science* **309**, 752 (2005).
- [7] K. Fukui, Y. Namai, and Y. Iwasawa, *Appl. Surf. Sci.* **188**, 252 (2002).
- [8] Y. Namai, K. I. Fukui, and Y. Iwasawa, *Catal. Today* **85**, 79 (2003).
- [9] S. Gritschneider, Y. Namai, Y. Iwasawa, and M. Reichling, *Nanotechnology* **16**, S41 (2005).
- [10] S. Gritschneider and M. Reichling, *Nanotechnology* **18**, 044024 (2007).
- [11] S. Morita, R. Wiesendanger, and E. Meyer, *Noncontact Atomic Force Microscopy*, NanoScience and Technology (Springer-Verlag, Berlin, 2002).
- [12] R. García and R. Pérez, *Surf. Sci. Rep.* **47**, 197 (2002).
- [13] F. J. Giessibl, *Rev. Mod. Phys.* **75**, 949 (2003).
- [14] S. Fabris, G. Vicario, G. Balducci, S. de Gironcoli, and S. Baroni, *J. Phys. Chem. B* **109**, 22860 (2005).
- [15] N. Suehira, Y. Tomiyoshi, Y. Sugawara, and S. Morita, *Rev. Sci. Instrum.* **72**, 2971 (2001).
- [16] I. Horcas *et al.*, *Rev. Sci. Instrum.* **78**, 013705 (2007).
- [17] T. R. Albrecht, P. Grütter, D. Horne, and D. Rugar, *J. Appl. Phys.* **69**, 668 (1991).
- [18] M. Abe, Y. Sugimoto, O. Custance, and S. Morita, *Appl. Phys. Lett.* **87**, 173503 (2005).
- [19] N. Oyabu, O. Custance, I. Yi, Y. Sugawara, and S. Morita, *Phys. Rev. Lett.* **90**, 176102 (2003).
- [20] L. N. Kantorovich and T. Trevethan, *Phys. Rev. Lett.* **93**, 236102 (2004).
- [21] N. Oyabu, P. Pou, Y. Sugimoto, P. Jelinek, M. Abe, S. Morita, R. Perez, and O. Custance, *Phys. Rev. Lett.* **96**, 106101 (2006).
- [22] L. Ottaviano, B. Ressel, C. DiTeodoro, G. Profeta, S. Santucci, V. Cháb, and K. C. Prince, *Phys. Rev. B* **67**, 045401 (2003).
- [23] F. J. Giessibl, *Phys. Rev. B* **56**, 16010 (1997).
- [24] First mechanical resonant frequency, oscillation amplitude, spring constant, and Q value were 173788 Hz, 51 Å, 37.5 N/m, and 175 000 for Fig. 1(a), and 172 207 Hz, 51 Å, 36.5 N/m, and 194 000 for Figs. 1(b), 2, and 3, respectively.